Resource-Efficient Simulation Framework for Accurate UWB Antenna System Design

Jelle Jocqué, Quinten Van den Brande, Stijn Luchie, Ben Van Herbruggen, Eli De Poorter, Jo Verhaevert,
Sam Lemey, *Member, IEEE*, Patrick Van Torre, *Member, IEEE*, Hendrik Rogier, *Senior Member, IEEE*

***Abstract*—Next-generation Ultra-Wideband (UWB) applications require high–performance and fully-integrated UWB antenna systems to guarantee accurate localization and sensing in challenging Internet of Things (IoT) environments. This paper proposes an entire system-level simulation framework that accelerates the design and optimization of integrated UWB antenna systems for various IoT applications by accurately predicting the effects of the entire system integration environment and enabling time-efficient optimization of system-level metrics. These metrics include the System Fidelity Factor and the Distance Estimation Error in full 3D, which are required to minimize orientation-specific pulse distortion and phase-center variation. To reconcile fast and accurate system-level performance prediction with reduced computational resources, the UWB link is partitioned, enabling the combination of standalone full-wave antenna simulations, UWB front-end circuit models, and UWB wireless channel models considering all antenna and circuit imperfections. Moreover, this simulation framework is the first to include the Huygens' field equivalence principle to efficiently and accurately model the entire system environment, crucial to ensure high-performance UWB antenna systems for integrated IoT applications. To validate the simulation framework, an extensive time-domain measurement campaign was performed on a representative UWB link, including multiple integration platforms. Simulation and measurement results correspond well and show that the presence of the actual integration platform significantly impacts the system performance along different orientations. The simulation framework is several orders of magnitude faster than what is currently achievable with conventional electromagnetic field simulators and facilitates the development of high–performance and fully integrated UWB systems that satisfy the needs of demanding IoT applications.**

***Index Terms*—ultra-wideband (UWB), transfer function, link performance merits, simulation framework, integration platforms**

I. INTRODUCTION

ULTRA-WIDEBAND (UWB) systems play a pivotal role in Industry 4.0, Smart Buildings, eHealth, automotive and Internet of Things (IoT) applications for high-quality localization, tracking, ranging and sensing. The absence of Global Navigation Satellite System (GNSS) signals within indoor factory environments has led to alternative indoor Real-Time Locating Systems (RTLS) to provide precise and robust location information. Numerous RTLS have been explored, including those based on infrared radiation, ultrasound, Bluetooth and WiFi [1]. Time-of-Arrival (ToA) and Angle-of-Arrival (AoA) based UWB RTLS have received significant attention by both the academic and industrial world in the last decade. This is because UWB systems rely on bursts of (sub)nanosecond pulses to transmit information and, hence, exhibit high immunity to both multipath and narrowband interference. In data-driven smart factories, for instance, location information has become crucial for workflow optimization [2], resource tracking [3], safety management [4] and autonomous robot navigation [5]. In addition, precise localization is crucial for IoT devices, providing features such as preference management, privacy and security [6]. Current commercial UWB applications claim sub-decimeter and a 10–30-cm positioning accuracy in indoor LOS and NLOS conditions, respectively [6]. However, next-generation UWB applications such as UWB radar for gesture recognition [7], monitoring individuals [8] and vital signs [9], require more reliable and more accurate UWB systems. Moreover, the existing solutions are becoming inadequate due to the harsh and challenging propagation conditions, high levels of interference, and the substantial number of IoT devices requiring service within the smart factory environment [3]. In addition, to accelerate the large-scale roll-out of these next-generation UWB systems and to enable unobtrusive integration in a wide variety of everyday objects [10], [11], there is a strong need for co-design, co-optimization and co-integration of the UWB system with the entire system environment. The entire system environment encompasses all components, interactions, and external factors that can affect the functionality and performance of the UWB system in actual deployment conditions. The integration platform is a critical component in this environment. Its influence on the UWB transmit and receive antenna system can lead to inadequate impedance matching, undesired coupling, and deformation of the antenna radiation pattern.

The use of (sub)nanosecond pulses and the advanced seamless integration in demanding next-generation IoT applications urge the need for a holistic system-level approach for the design and optimization of such highly integrated UWB systems, and more specifically their transmit (Tx) and receive (Rx) antenna modules to guarantee high performance in challenging real-life deployment conditions. In addition to enforcing specifications for conventional frequency-domain antenna performance indicators, time-domain performance optimization is

---

Manuscript received April 1, 2024; revised November 14, 2024; accepted December 3, 2024. *(Corresponding author: Jelle Jocqué.)*

Jelle Jocqué, Stijn Luchie, Ben Van Herbruggen, Eli De Poorter, Jo Verhaevert, Sam Lemey, Patrick Van Torre and Hendrik Rogier are with the Department of Information Technology, Ghent University/imec, 9052 Ghent, Belgium (e-mail: jelle.jocque@ugent.be).

Quinten Van den Brande is with TMC, 5656 AG Eindhoven, The Netherlands.

essential to minimize pulse distortion [12]. Frequency-domain antenna performance indicators include antenna impedance matching, which aims at minimizing the magnitude of the antenna's reflection coefficient or maximizing the antenna's return loss. They also include the antenna radiation characteristics in terms of its antenna gain, radiation efficiency and the antenna-coupling between neighboring elements or nearby structures, aimed at maximizing isolation. Time-domain performance is characterized by the impulse response, which is crucial for investigating the System Fidelity Factor (SFF) [13] and the Distance Estimation Error (DEE) [14]. In this process, the transmit and the receive chain should be included in the simulation [15], [16], as they have a significant influence on the performance of UWB systems for localization and sensing [17]. Moreover, not only time-domain performance along a single main direction, such as broadside, should be analyzed, but also more comprehensive orientation-specific system-level figures of merit, such as the angle-dependent SFF and the DEE in full 3D, to prevent antenna-induced orientation-specific ranging bias [18]. While digital predistortion can be used to increase pulse fidelity [19], it is only useful if the antenna-induced pulse distortion is constant over its entire field-of-view. Besides introducing orientation-specific pulse distortion, inappropriate UWB antenna design might introduce phase-center variations (angle-dependent offset between the antenna reference point and the real incidence point [20]) leading to systematic errors, which can drastically impact UWB localization and sensing applications [21]. Finally, the effects of the entire system environment should be taken into account. Antenna-to-integration-platform coupling may cause frequency-dependent distortion of the antenna radiation pattern, severe detuning and higher mutual coupling in multi-antenna systems [22]. While high mutual coupling between the Rx and the Tx antenna reduces the range in UWB radar applications [9], antenna radiation pattern deformation and detuning will lead to orientation-specific pulse distortion and phase-center variations, drastically affecting UWB localization and sensing performance [22], [23].

In [24], a custom UWB system with integrated omnidirectional chip antenna and UWB transceiver (DWM1000) is placed on top of a drone for 3D localization of sensor nodes. A lightweight machine-learning-based error-correction model was applied, resulting in an improvement in localization error with an upper-boundary of 21 cm. However, the measured ranging error as a function of azimuth angle is showing outliers with a localization error up to 85 cm due to the system environment. These effects may be significantly reduced by co-design and co-optimization of the UWB localization system with the entire system environment. Yet, no simulation tools currently exist to efficiently and simultaneously optimize the UWB system for these time-domain and system-level metrics in full 3D while including the entire system environment. This makes the design, optimization and integration of next-generation UWB applications for highly accurate localization and sensing very challenging.

In this paper, a novel simulation framework is proposed to enable highly accurate, time-efficient system-level analysis and optimization of UWB antenna systems for localization and sensing in harsh IoT environments by incorporating all relevant system environment side effects. By first performing standalone full-wave and/or circuit simulations of each separate link component and, subsequently, efficiently integrating them in the simulation framework to characterize the complete system performance, a modular approach is obtained that allows for light-weight simulations with extensive design flexibility. In addition, leveraging the Huygens' field equivalence principle enables us to combine standalone full-wave simulations with a 3D ray tracer, based on the shooting and bouncing rays (SBR) technique, to include integration platforms in a time-efficient way. The simulation framework can be exploited for a thorough analysis of the complete UWB system, providing insight in the impact of each design choice, but also for their optimization [25], [26]. This ensures reliable and high performance after deployment in challenging real-life conditions. Note that the modular simulation framework also allows measurement results to be included for co-optimization. This approach allows us to minimize phase-center variations and pulse distortion throughout the entire system for all possible directions, from the UWB transmitter to the receiver, while accounting for all relevant system environment effects, as well as antenna and circuit imperfections. This is done for all relevant orientations of the Tx and Rx antennas, thereby effectively mitigating orientation-specific ranging bias, which is crucial for high-performance UWB antenna systems. The simulation framework's accuracy is validated by dedicated time-domain measurements, both in standalone conditions as well as when the UWB module is deployed on a metal plate (mimicking the impact of large metal objects such as ship hulls, metal racks or the body of a car) and on a robotic integration platform. Simulation and measurement results correspond very well and prove that the presence of such integration platforms can drastically impact system performance. In addition, the presented simulation framework facilitates UWB system designers in assessing the influence of the integration platform on the overall system performance and ascertaining the need for additional precautions. Furthermore, the simulation framework performance is benchmarked against commercially available solvers, showing a significant reduction in CPU time.

Specifically, the main contributions of the paper are the following:

1) This paper presents a modular system-level simulation framework, incorporating all antenna and circuit imperfections in the UWB wireless link by leveraging standalone full-wave antenna simulations, UWB front-end circuit models, and UWB wireless channel models.
2) It is the first paper that includes the entire system environment in the UWB wireless link by leveraging the Huygens' field equivalence principle.
3) It includes non-linear RF front-end effects and its impact on Two Way Ranging (TWR) performance.
4) It allows minimization of orientation-specific pulse distortion and phase-center variation by jointly optimizing system-level metrics, such as SFF and DEE, in full 3D.

The remainder of this paper is organized as follows. Section II provides an overview of the related work involving simulation frameworks focusing on UWB electronic circuitry and/or antenna links. Section III outlines the simulation framework architecture and elaborates on the UWB system link decomposition. In Section IV, the simulation accuracy, timing and performance are validated and benchmarked against commercial solvers. Next, in Section V, a real UWB system is evaluated on ranging accuracy and a more realistic robotic integration platform is briefly discussed. Finally, the conclusions are presented in Section VI.

II. RELATED WORK

Next-generation UWB-based IoT applications require wireless systems that are simultaneously optimized for time-domain and system-level metrics in full 3D, while including the entire system environment to reconcile high performance with seamless integration. To fulfill this challenging set of design requirements, a system-level approach needs to be adopted to ensure excellent performance in the frequency, time and spatial domains, while also taking into account fabrication, integration, cost and size aspects. To speed up simulation time and shorten the design cycle of pulse-based UWB wireless systems, multiple system-level simulation frameworks have been proposed in literature [27]–[35]. An overview of these simulation frameworks is given in Table I. First, we examine the simulation of active electronics in the UWB link. This is succeeded by the inclusion of antenna effects in the frequency domain, followed by frameworks that focus on the time domain and eventually also system-level metrics. Finally, there is a brief discussion of frameworks using Machine Learning (ML) techniques for the design and optimization of antennas.

In [27] and [36], a comprehensive simulation framework is proposed to accurately simulate a complete UWB link in Matlab and Keysight's Pathwave Advanced Design System (ADS), including the analog front-ends, digital back-ends and channel effects. Whereas this paper initially focused on UWB indoor localization, the generality of the simulation framework also enables predicting the performance of UWB radar systems [37], [38]. In particular, the simulation framework was leveraged to accurately predict the performance limitations of a pulse-based three-dimensional through-wall imaging radar. It allows analyzing various effects, such as signal quality, pulse shape and environmental characteristics. It was fully validated using an FPGA-based UWB radar platform. While this simulation framework focused on the active electronics and put less emphasis on antenna-induced orientation-specific pulse distortion and phase-center variations, other dedicated simulation frameworks have been presented that focus more on antenna effects in the UWB link [28], [30]–[33]. These simulation frameworks speed up the frequency-domain optimization of UWB antennas, but only [30]–[33] support joint optimization in the time domain as required for pulse-based UWB ranging and sensing.

In [30], a factored broadband channel model for the optimization of UWB antenna links with real, dispersive antennas, was proposed. It was verified by a Method-of-Moments (MoM) technique and analyzes the effect of transmitter and receiver impedances on achievable link performance, clearly demonstrating the advantage of antenna-IC co-optimization. However, it does not consider angle-dependent pulse distortion and phase-center variations, which are required for the system-level metrics in full 3D. In [33], a novel method was proposed to analytically model the angle-dependent pulse distortion of planar UWB antennas. Based on time-domain antenna measurements, the antenna's aperture field distribution is estimated. Next, the proposed method relates the incident transient field to the antenna output pulse in receive mode, and the antenna input pulse to the transient radiated fields in transmit mode. It is validated by comparing the measured received pulse of three different UWB antennas to the model. By leveraging this analytical model, orientation-specific pulse distortion can be minimized and UWB radio designers are given prior knowledge of the remaining distortion. Yet, the analytical approach impedes simulating more advanced UWB

TABLE I
OVERVIEW OF EXISTING UWB SIMULATION FRAMEWORKS.

Simulation Framework	**Antenna**					**System-Level Metrics**		**RF Front-Ends**	**System Environment**
	Full-Wave	**Analytical**	**Frequency Domain**	**Time Domain**	**Full 3D**	**SFF**	**DEE**		
[27]								✓	
[28]		✓	✓					✓	
[29]	✓		✓		✓				
[30]	✓		✓	✓					
[31]	✓		✓	✓				✓	
[32]		✓	✓	✓	✓				
[33]		✓	✓	✓	✓	✓			
[34]	✓		✓	✓	✓	✓			
[35]	✓		✓	✓	✓	✓			
This Work	✓		✓	✓	✓	✓	✓	✓	✓

antennas and does not allow including RF front-end imperfections and the entire system environment. In [31], a general simulation framework is proposed to analyze the impact of the UWB antennas on the system performance for a pulse-based physical-layer scheme. To enable a more detailed analysis compared to [30] and [33], full-wave antenna simulations in either WIPL-D [39] or in CST Microwave Studio (MWS) are leveraged [40]. WIPL-D utilizes the MoM applied to surface integral equations employing higher-order basis functions and a quadrilateral mesh for accurate analysis of complex geometries, particularly in antenna design and scattering problems. CST MWS employs various numerical methods, including the finite integration technique in both Time Domain and Frequency Domain as well as finite element and integral equation solvers. These methods are used to simulate electromagnetic fields in 3D structures, making it ideal for computer-aided UWB antenna design and optimization. In doing so, the simulation framework can be used to discover the main cause of pulse distortion in a given UWB link, while also supporting optimization of UWB antennas in the time domain, but not in full 3D. Moreover, no system-level metrics are discussed, and it is not possible to include the entire system environment.

In recent years, ML is exploited more and more to design and optimize UWB antenna systems [29], [34], [35]. In [41], a comprehensive overview of advanced computational methods is given for the analysis, synthesis, and optimization of UWB antennas. These methods are subdivided into four categories, being artificial neural networks, genetic algorithms, particle swarm optimization and hybrid techniques. While most of the work on ML-based UWB antenna optimization focuses on frequency-domain parameters, [34] and [35] also include time domain parameters in the multi-objective optimization process. Recently, in [29], a ML-assisted electromagnetic modelling framework for UWB antennas was published to further speed up UWB antenna development. To validate the simulation framework, a dual-element and quad-element UWB Multiple Input Multiple Output (MIMO) antenna system were designed and measured, demonstrating good agreement and a significant reduction in optimization time. Yet, both designs were only optimized for frequency-domain parameters, and do not take the orientation-specific pulse distortion and phase-center variation into account. In [42] and [43], a multistage collaborative machine learning (MS-CoML) method and a deep reinforcement learning (DRL) algorithm are proposed, respectively, for the design and optimization of antennas and antenna arrays, but not for UWB purposes. In summary, ML techniques can be useful for the optimization of UWB antennas, but they do not yet provide any insights into the orientation-specific system-level figures of merit, which are essential for UWB antenna system design.

III. SIMULATION FRAMEWORK

A. *Simulation Framework Architecture*

The simulation framework first partitions the UWB system into a transmitter part (Tx system), receiver part (Rx system) and the wireless propagation channel, as shown in Fig. 1. The transmit system is further subdivided into a pulse generator and a transmit chain, comprising a variety of microwave components, such as filters, power amplifiers, and a transmit antenna. Similarly, the receive system is subdivided into a correlator and a receive chain, comprising a variety of microwave components such as filters, low-noise amplifiers and a receive antenna. The antenna link can be implemented by any pair of transmit and receive antennas, each with arbitrary orientations,

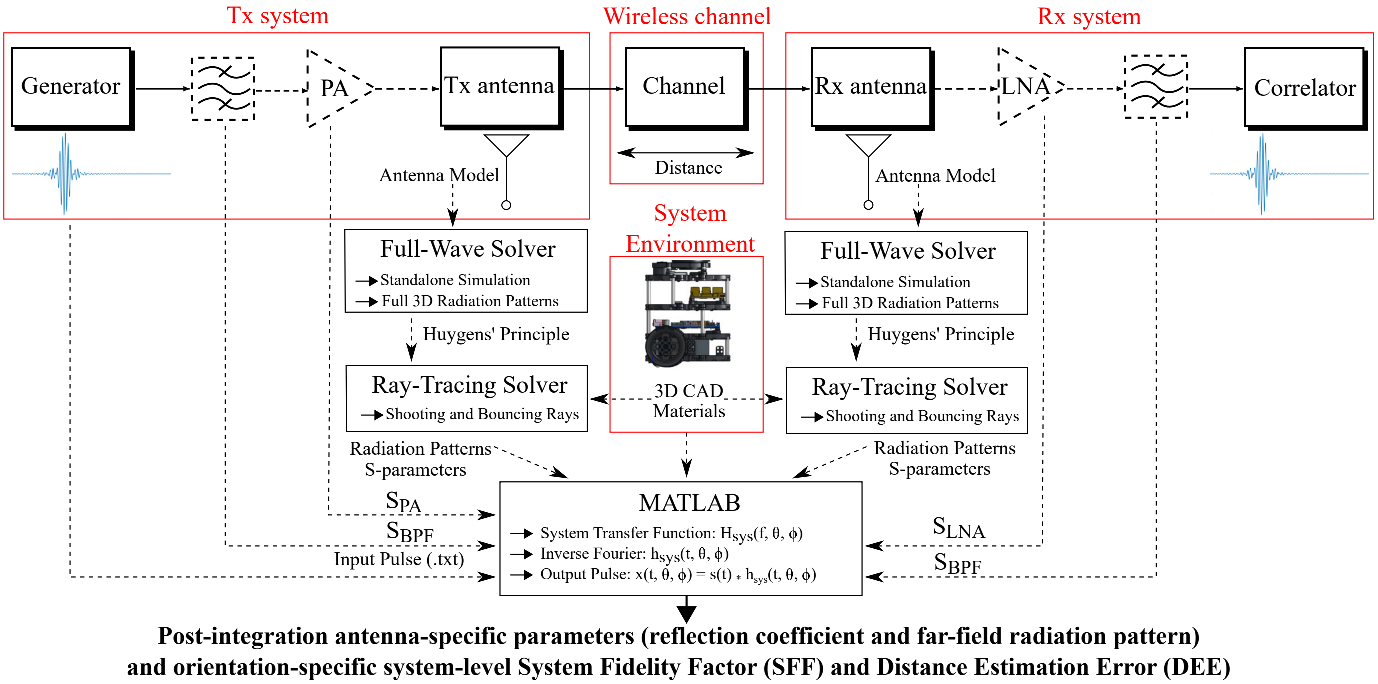

Fig. 1. High-level modular overview of the complete UWB system as described in the proposed simulation framework including the transmitter part (Tx system), receiver part (Rx system), the entire system environment, and the wireless propagation channel.

and a propagation channel, which may be a free-space link or a multipath channel. Therefore, a modular approach is proposed in Fig. 1 to facilitate efficient and agile system-level simulations.

To characterize the performance of UWB systems, given a certain predefined excitation pulse, a thorough frequency- and time-domain analysis of the complete system is required. By calculating the received pulse and comparing it to the transmitted pulse, a wide variety of system-level metrics are extracted, such as the SFF and the DEE. The SFF characterizes the amount of pulse distortion introduced by the entire antenna system [13], [44]. In turn, the amount of ranging bias is quantified by the DEE, comparing the estimated ToA for different configurations to the ToA in boresight of the antenna system [14].

Each component is considered linear (active components, appropriately biased, may be included through small-signal analysis) and is characterized by its S-parameters, calculated by either a circuit or full-wave solver, or a combination of both. Subsequently, the S-parameters of every component are transformed into ABCD-parameters so that they can be cascaded to determine the complete orientation-specific system transfer function (Fig. 2), defined as $H_{sys}(f,\theta,\phi)=\frac{V_2}{V_1}$, based on

$$\begin{bmatrix} V_1 \\ I_1 \end{bmatrix} = \begin{bmatrix} A & B \\ C & D \end{bmatrix} \begin{bmatrix} V_2 \\ -I_2 \end{bmatrix} \tag{1}$$

with V_1 the input voltage, I_1 the input current, V_2 the output voltage, I_2 the output current and A, B, C and D the elements of the ABCD matrix:

$$\begin{cases} A = \frac{(1+S_{11})(1-S_{22})+S_{12}S_{21}}{2S_{21}} \\ B = Z_0\frac{(1+S_{11})(1+S_{22})-S_{12}S_{21}}{2S_{21}} \\ C = \frac{1}{Z_0}\frac{(1-S_{11})(1-S_{22})-S_{12}S_{21}}{2S_{21}} \\ D = \frac{(1-S_{11})(1+S_{22})+S_{12}S_{21}}{2S_{21}} \end{cases} \tag{2}$$

with S_{11} the input reflection coefficient, providing a measure for the input matching, S_{21} the forward transmission coefficient, S_{12} the reverse transmission coefficient, both providing a measure for the insertion loss, S_{22} the output reflection coefficient, providing a measure for the output matching, and Z_0 the reference impedance of the S-parameters [45].

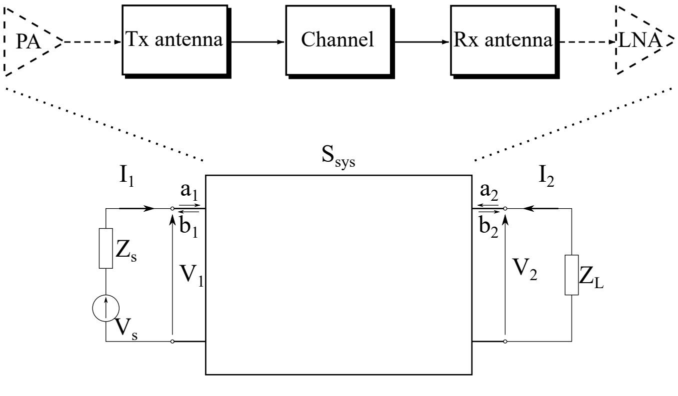

Fig. 2. Graphical representation of the UWB system transfer function.

For a free-space channel with direction of departure at the transmitter along the unit vector $\mathbf{u}$ and direction of arrival at the receiver along $\mathbf{u}$, the transmission coefficient of the channel (Fig. 3) $S_{channel,21}$ at frequency f is given by

$$\begin{aligned} S_{channel,21} = \left(1-|\Gamma_{Rx}|^2\right)\left(\frac{Z_L}{Z_L+Z_R}\right) \\ \left(\frac{-2\jmath\lambda}{Z_c}\right)\left(\mathbf{F_T}(\mathbf{u})\cdot\mathbf{F_R}(-\mathbf{u})\right)\left(\frac{e^{-\jmath kr}}{r}\right) \\ \left(\frac{1}{Z_T+Z_S}\right)\left(1-|\Gamma_{Tx}|^2\right), \end{aligned} \tag{3}$$

with Z_L the load impedance, Z_R the input impedance of the receive antenna, Z_c the free-space impedance, Z_T the input impedance of the transmit antenna, Z_S the internal impedance of the source generator, $\lambda = c/f$ the free-space wavelength, c the speed of light, f the frequency, $\jmath$ the imaginary unit, k the wave number and r the distance between both antennas [15]. $\mathbf{F}(\mathbf{u})$ is the radiation vector for the direction defined by $\mathbf{u}$, of both transmit (subscript T) and receive antenna (subscript R). In addition, owing to the modularity of the system, instead of a free-space channel, also multipath channels (simulated or measured) may be included in the UWB link by replacing (3) by a similar multipath-propagation formula.

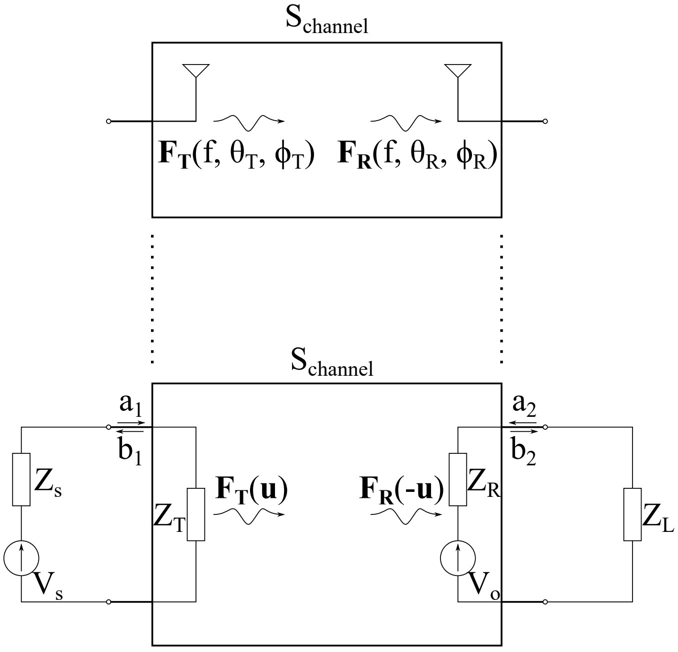

Fig. 3. Equivalent circuit of the channel between the transmit antenna (left) and the receive antenna (right).

Performing full-wave simulations of the complete antenna link for different antenna orientations and separations quickly becomes computationally intensive. Therefore, the antenna link should be decomposed to enable link simulations based on the individual radiation patterns of the standalone antennas. To this end, a circuit equivalent model is used for the antenna link without additional peripheral circuitry, as proposed in [15]. It enables translating, rotating or even replacing one of the antennas in the link without having to resimulate the complete link for each relevant deployment orientation.

Finally, the discretization of continuous time-domain signals and frequency-domain parameters during simulations impacts not only the computational workload, but also the system-level parameter accuracy. The UWB spectrum is generally defined within the frequency range of 3.1 GHz to 10.6 GHz [46], which results in a sample rate of at least 21.2 GHz, as prescribed by the Nyquist Theorem. Although this theorem establishes a minimum sample rate, a widely accepted rule of thumb suggests sampling at a rate substantially greater than twice the bandwidth, typically recommending a sampling rate of 5 to 10 times the bandwidth to obtain more samples per period of the waveform, resulting in higher accuracy with straightforward processing. In addition, UWB systems rely on (sub)nanosecond pulses and, therefore, a guideline is to select the time step $\delta t < 10$ picoseconds (ps) [47], corresponding to a sampling frequency above 100 GHz.

B. Transmit Chain

The transmit chain consists of different components such as the pulse generator, filters, power amplifiers, and the transmit antenna. The representative transmit system in the modular approach, outlined in Fig. 1, is compliant with the latest UWB transmitter architectures [48]. In the proposed simulation framework, the generated pulse may be any predefined pulse, such as a root-raised-cosine pulse, characterized by

$$s(t) = \frac{2\cos(2\pi f_0 t)}{\pi\sqrt{T_p}} \frac{\cos(1.5\pi t/T_p) + \frac{\sin(0.5\pi t/T_p)}{2t/T_p}}{1 - (2t/T_p)^2}, \tag{4}$$

with f_0 the pulse carrier frequency and T_p the pulse width, which is defined by the IEEE 802.15.4-2020 standard [46]. It may also be a customized pulse or a measured pulse described by a set of time-series data. Next, the simulated or measured S-parameters of active components, which are set to their correct operating point by applying appropriate DC bias voltages, can be incorporated using small-signal analysis. The latter refers to the study of how these components respond to small input signals around their operating point, allowing us to analyze their behavior with linear approximations. This approach allows designers to co-design and optimize the transmit chain, utilizing advanced circuit simulators such as Keysight's Pathwave ADS. Next, the transmit antenna system is integrated into the simulation framework by incorporating its radiation patterns and its S-parameters, which can be obtained either through a full-wave solver, such as CST MWS, or by direct measurements.

C. Receive Chain

The receive chain is typically composed of a correlator, filters, low-noise amplifiers and a receive antenna. The representative modular receive chain, considered in Fig. 1, is compliant with the latest UWB receiver architectures [49]. When the receive antenna is excited by an incident electromagnetic plane wave in a free-space environment without multipath, an open-circuit voltage [50], [51]

$$V_o(\mathbf{u}) = \frac{-2\jmath c}{Z_c f}\left(\mathbf{F}_R(-\mathbf{u}) \cdot \mathbf{E}^{inc}\right) \tag{5}$$

is induced, with $\jmath$ the imaginary unit, c the speed of light, Z_c the free-space wave impedance, f the frequency, $\mathbf{F}_R(-\mathbf{u})$ the radiation vector of the receive antenna along direction $\mathbf{u}$ and $\mathbf{E}^{inc}$ the electric field of a plane wave impinging from that direction. Similar to the transmit chain, simulated or measured S-parameters of the active components and the receive antenna, as well as the antenna's radiation patterns can be imported into the simulation framework.

To calculate the output pulse, the system impulse response $h_{sys}(t, \theta, \phi)$ is computed by performing an inverse Fourier transformation on the system transfer function $H_{sys}(f, \theta, \phi)$. The output pulse $x(t, \theta, \phi)$ is then obtained as

$$x(t, \theta, \phi) = s(t) * h_{sys}(t, \theta, \phi), \tag{6}$$

with $s(t)$ the input pulse and $*$ the convolution operator. Once the output pulse is known, all relevant system-level characteristics are determined by correlating the output-pulse envelope with the input-pulse envelope. The orientation-specific SFF and DEE are of particular interest in the context of UWB systems for localization and sensing, as they characterize the localization system accuracy. The SFF is obtained by

$$\mathrm{SFF}(\theta, \phi) = \max_t \left| \frac{\int_{t_0}^{t_n} s(\tau)x(\tau + t, \theta, \phi)d\tau}{\sqrt{\int_{t_0}^{t_n} s^2(\tau)d\tau \int_{t_0}^{t_n} x^2(\tau, \theta, \phi)d\tau}} \right|, \tag{7}$$

with $s(\tau)$ the input pulse as a function of time τ, $x(\tau+t, \theta, \phi)$ the time-shifted (by time t) output pulse as function of time τ, ϕ and θ the azimuth and polar angle in a spherical coordinate system, respectively, and t_0 and t_n the first and last time sample, respectively [13]. The denominator normalizes the cross-correlation in the numerator, resulting in an SFF value between 0 and 1. The DEE is obtained by

$$d_{est,e}\left(\theta, \phi\right) = \left(t_{max}\left(\theta, \phi\right) - t_{max}\left(0, 0\right)\right)c, \tag{8}$$

with c the speed of light and $t_{max}(\theta, \phi)$ and $t_{max}(0, 0)$ the time at which the SFF becomes maximal for (θ, ϕ) and broadside, respectively.

D. Wireless Channel and System Environment

The previously described antenna link decomposition requires a standalone full-wave simulation of both the transmit and receive antenna in a free-space environment, providing us the S-parameters that model antenna matching and mutual coupling between neighboring antenna elements, in case of an antenna array, and the standalone full 3D radiation patterns, via their angle-dependent radiation vectors. However, when studying modern IoT systems in realistic scenarios, almost every application features a receive antenna and/or a transmit antenna integrated close to electronics, walls, ceilings, metal structures, etc. These integration platforms can severely and detrimentally affect the antenna performance [22]. The proposed simulation framework enables designers to incorporate the entire system environment into the system transfer function by importing the antenna models or measurements in a 3D ray tracer that is based on the SBR technique, with the inclusion of edge diffractions [52]. Therefore, a 3D CAD model and a material file of the integration platform need to be added to the simulation framework.

To accurately simulate these platform effects, the field equivalence principle is employed [53], allowing us to decompose the domain containing the antenna system from the platform [54]. Therefore, according to the Huygens' principle, along the closed surface forming the interface between the antenna system and the platform, virtual electric and magnetic current densities are introduced, corresponding to the tangential magnetic and electric fields on that boundary, generated or received by the antenna operating in the presence of the platform. The simulation framework iteratively approximates these tangential fields [55] by starting from the equivalent electric and magnetic currents produced by the antenna in stand-alone conditions as a zero-order approximation [56]. These can directly be derived from the far-field radiation pattern [57]. Then, a first-order estimate of the effect of the platform on the antenna system is derived by solving the field problem in the presence of the platform based on these sources. This field distribution, in turn, allows the simulation framework to refine virtual electric and magnetic currents on the Huygens' surface and to start a next iteration based on these new first-order approximations to model the antenna interaction with the platform in an even more accurate manner. We continue iterating until the Huygens' sources have converged, thereby fully taking into account the effect of the platform on the antenna system. Moreover, owing to the modularity of the system, also multipath channels (simulated or measured) may be included in the link, for example, to analyze the performance of IoT nodes with UWB localization and sensing capabilities in an industrial environment [58].

IV. VALIDATION: A REPRESENTATIVE UWB LINK

A. Antenna Link and Measurement Setup

To validate the theory postulated in the previous section, the proposed modular design simulation framework is applied to simulate a representative UWB link. This link consists of a hemispherical transmit antenna, serving as the anchor node, and an omnidirectional receive antenna, acting as the tag node. The transmit antenna is a highly efficient coupled half-mode cavity-backed slot antenna implemented in stacked air-filled substrate integrated waveguide (SIW) technology [25], while a monopolar spline antenna [59] is used as receive antenna. The transmit antenna is fixed in the setup and the receive antenna is mounted on the rotating robot arm, as depicted in Fig. 4. When deployed on the NSI measurement system in the anechoic chamber, both antennas are spaced 2.34 m apart in free space (corresponding to a delay of 7.8 ns). The described UWB link is now simulated and measured using this monopolar spline antenna, both in free space and in front of a circular metal plate with a diameter of 43.5 cm and a thickness of 1.65 mm. This metal plate is specifically chosen to mimic and represent a typical metal integration platform, such as a robotic platform, a ship hull, or a car roof [26].

A modulated root-raised-cosine pulse is transmitted, characterized by (4) with $f_0 = 4.4928$ GHz the pulse carrier frequency and $T_p = 2$ ns the pulse width, resulting in a pulse bandwidth of 499.2 MHz [46]. To measure the proposed system, a dedicated time-domain measurement setup, depicted in Fig. 5, is constructed inside an anechoic chamber, composed of a Keysight M8195A Arbitrary Waveform Generator (AWG) (with a sampling rate of 65 GSa/s), to generate the input pulse, and a LabMaster 10-65Zi-A Real-Time Oscilloscope (RTO) (sampling at 160 GSa/s) from Teledyne LeCroy, to measure the received pulses. The noise introduced by the RTO is also included in the simulation framework as additive white Gaussian noise.

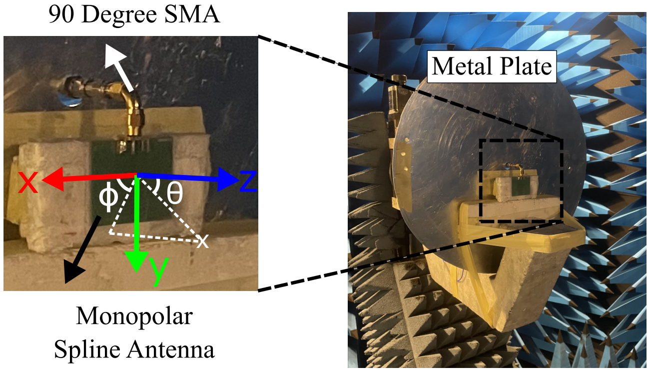

Fig. 4. To measure the orientation-specific impact of an integration platform, a monopolar spline antenna is placed on a rotating robot arm in front of a circular metal plate, representing a metal integration platform.

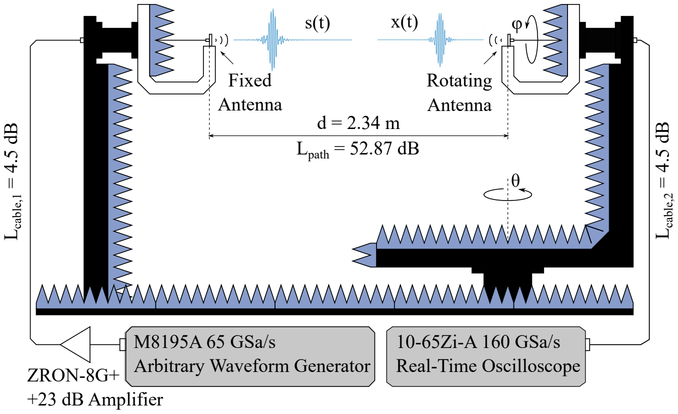

Fig. 5. Measurement setup for the time-domain measurements in free-space conditions with a fixed transmit antenna and a rotating monopolar spline receive antenna [14].

The resulting time and frequency domain settings are given by

$$\begin{cases} f_s = 160 \text{ GHz} \\ \delta f = \frac{1}{t_{max}} = \frac{1}{20 \text{ ns}} = 50 \text{ MHz} \\ t_{max} = 20 \text{ ns} \\ \delta t = \frac{1}{f_s} = \frac{1}{160 \text{ GHz}} = 6.25 \text{ ps}, \end{cases} \tag{9}$$

with f_s and δf the sampling frequency and the frequency step, respectively, and t_{max} and δt the maximum observation time and the time step, respectively.

B. Frequency Domain: S-parameters

The magnitude of the reflection coefficient of both antennas, expressed in dB and with respect to 50 Ω, is depicted in Fig. 6. Both the transmit and the receive antenna cover the IEEE 802.15.4z channel 3 frequency band from 4.2432 GHz to 4.7424 GHz [46].

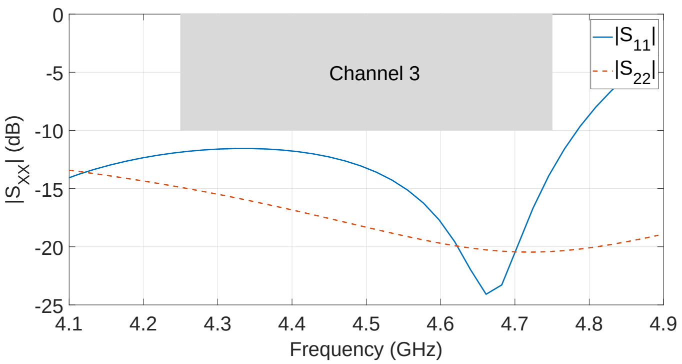

Fig. 6. Magnitude of the simulated reflection coefficient in dB, with respect to 50 Ω, of the fixed transmit antenna $|S_{11}|$ and the receive antenna $|S_{22}|$.

Next, the magnitude of the system transfer function of the antenna link $|H_{sys}(f, \theta, \phi)|$ in dB at the carrier frequency of 4.4928 GHz, as a function of the angle θ in both the xz-plane ($\phi = 0°$) and yz-plane ($\phi = 90°$) of the rotating monopolar spline antenna, is depicted in Fig. 7. Moreover, the frequency dependence of the system transfer function within the [4.2432; 4.7424 GHz] IEEE 802.15.4z channel 3 frequency band is also shown in Fig. 7, represented using a lighter color tone.

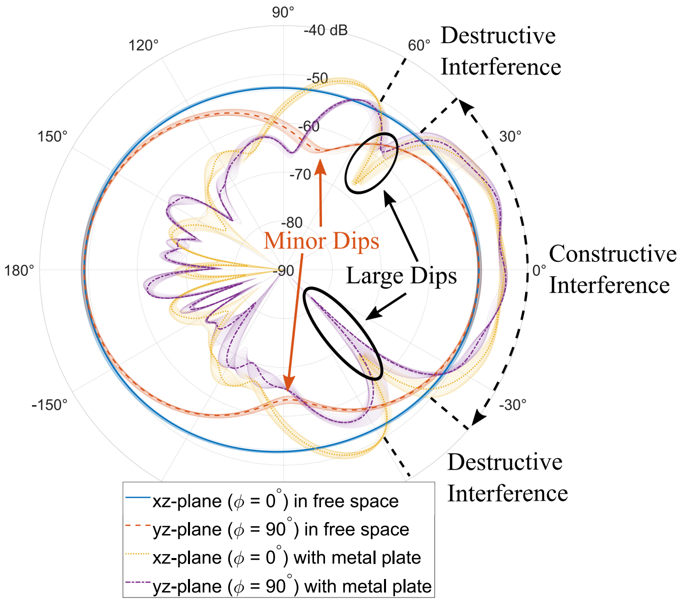

Fig. 7. Magnitude of the simulated system transfer function $|H_{sys}(f, \theta, \phi)|$ in dB within the [4.2432; 4.7424 GHz] IEEE 802.15.4z channel 3 frequency band, for both the xz-plane ($\phi = 0°$) and yz-plane ($\phi = 90°$), for the monopolar spline antenna along different rotations θ (Fig. 5) in free space and when deployed 48 mm in front of a metal plate.

As expected, the antenna link features a fairly constant magnitude of the system transfer function in both planes in free space. The minor dips at 90° and -90° in the yz-plane originate from the torus-shaped radiation pattern of the monopolar spline [59]. Subsequently, the antenna link was analyzed with the monopolar spline antenna deployed in front of a metal plate. The presence of the integration platform has a significant impact on the system transfer function, as it leads to constructive or destructive interference for certain angles. On the one hand, an increase in $|H_{sys}(f, \theta, \phi)|$ is noticed between 30° and -30°, because of constructive interference. On the other hand, multiple large dips are present in the xz-plane and yz-plane plane due to destructive interference between the direct wave and the reflected wave. In addition, there is much more variation in $|H_{sys}|$ than in free space. This can be attributed to the large electrical size of the integration platform, giving rise to a more irregular interference pattern with significant fluctuations.

C. Time Domain: SFF and DEE

In Fig. 8, we evaluate both the simulated and measured SFF of the antenna link by jointly analyzing the antennas' behavior across the frequency, time, and space domains in real-world deployment conditions. This is done for two scenarios: when the receive antenna is placed in free space and when it is positioned 48 mm in front of a metal plate, as shown in Fig. 4. Only the frontal hemisphere is depicted in Fig. 8 because of the presence of the metal plate behind the monopolar spline antenna. For the free-space link, the SFF is fairly constant and remains above 90% in the xz-plane. In general, an SFF of at least 80% is considered acceptable for most practical UWB systems, while higher precision UWB applications target an SFF above 90%. When the SFF drops below 50%, the output pulse is distorted such that it will no longer be recognized by the receiver [13]. In the yz-plane, minor dips can be observed around 90° and -90° in the simulated free-space SFF curve. These dips are caused by the torus-shaped radiation pattern of the monopolar spline antenna. Hence, as expected, in free-space conditions without interference, the pulse distortion remains minimal or negligible, except within the yz-plane from 60° to 90° and from -60° to -90°. However, when the antenna is deployed in front of the metal plate, severe pulse distortion can be observed at certain angles in the xz- and yz-plane, due to destructive interference. In particular, three prominent dips can be observed at approximately +50° and -50° in the xz-plane, and at -45° in the yz-plane, indicating significant pulse distortion. These three angles are labeled ”Pulse Distortion” and will be further explained in Subsection IV-D. In addition, a less prominent dip is observed at an angle of +50° in the yz-plane. This dip is labeled ”Phase-Center Variation” and will be further discussed in Subsection IV-E. The simulated and measured SFF for these four angles remain well above 50% and, therefore, it will not necessarily lead to information loss, but it will result in an orientation-specific range bias. The asymmetrical results observed in the yz-plane can be attributed to the asymmetrical placement of the monopolar spline antenna, coaxial cable and connector in the measurement setup, as shown in Fig. 4. In general, the SFF predicted by our simulation framework shows excellent consistency with the measurement results.

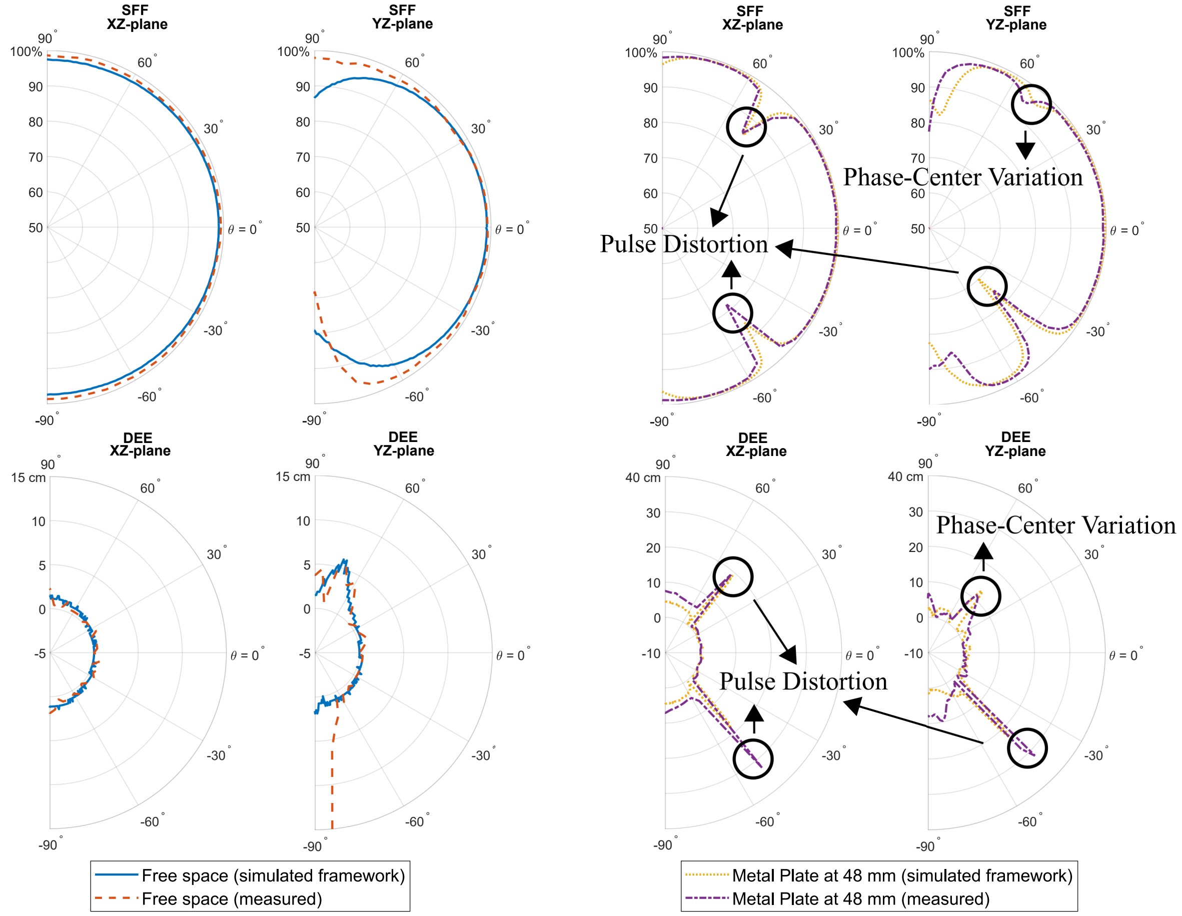

Fig. 8. SFF in % and DEE in cm for the xz-plane ($\phi = 0°$) and yz-plane ($\phi = 90°$), in free space (left) and 48 mm in front of a metal plate (right).

In addition to the SFF, the DEE is studied to analyze the angle-dependent ranging bias generated by the antenna link, due to pulse distortion and/or phase-center variation. The simulation framework and measured results of the DEE are shown in Fig. 8. Again, the DEE predicted by our simulation framework is in excellent agreement with the measured DEE in free-space, being close to 0 cm in both planes with a small increase from 60° to 90° in the yz-plane, as expected. The measured free-space DEE curve in the yz-plane shows a larger DEE at -90°, because of the position of the coaxial cable attached to the connector and the robotic measurement arm in the measurement setup. For the metal plate setup, there were three large dips for the SFF at +50° and -50° in the xz-plane and at -45° in the yz-plane. Along these angles, there is now a large increase in ranging bias, resulting in a DEE of about 20–30 cm in Fig. 8. Furthermore, a large spike is noticed at +50° in the yz-plane, whereas the corresponding SFF remains 95%, indicating that a phase-center variation is the cause for the large error in the estimated distance at this angle, as discussed into more detail in Subsection IV-E. At -90°, the deviation between simulation and measurement is again due to the position of the coaxial cable and the arm in the measurement setup. Overall, the DEE predicted by our simulation framework is in very good agreement with the measured results.

D. *Pulse Distortion*

In this part, we analyze the pulse distortion more in detail. Therefore, we compare the performance at broadside on the receive antenna to the performance at $\theta = -45°$ in the yz-plane (labeled with ”Pulse Distortion” in Fig. 8), for both the simulated and measured results. First, the measured normalized input pulse is depicted, together with both the simulated and measured normalized broadside output pulse, in Fig. 9.

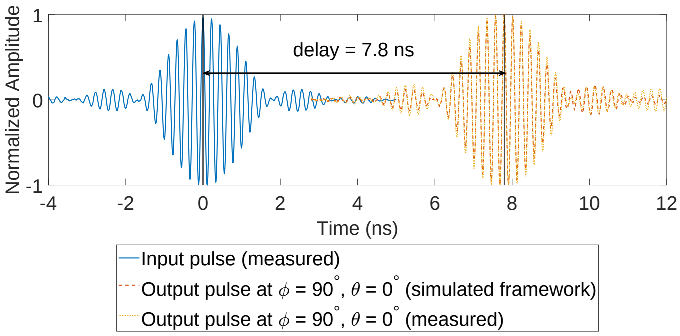

Fig. 9. Normalized amplitude of the measured input pulse, the simulated output pulse at broadside and the measured output pulse at broadside, with markers showing the 7.8 ns delay, corresponding with the 2.34 m distance between the antennas.

A very good agreement is obtained between the simulated broadside output pulse by the simulation framework and the measured broadside output pulse. Second, the same analysis for the distorted output pulse at $\theta = -45°$ in the yz-plane versus the input pulse is shown in Fig. 10(a). The pulse distortion is clearly visible here. To compare the simulated output pulse to the measured output pulse more in detail, the normalized envelope of these pulses is shown in Fig. 10(b). Notice that the joint contribution of both the direct path and the reflected path, depicted in Fig. 11, leads to a deformed pulse, which is also confirmed by the lower SFF value of 70% (simulation framework), compared to 97% (simulation framework) in free-space conditions, shown in Fig. 8. Although this value is still reasonable high, it can lead to a significant time shift for the peak of the pulse envelope, as shown in Fig. 10(b), resulting in much higher DEE values.

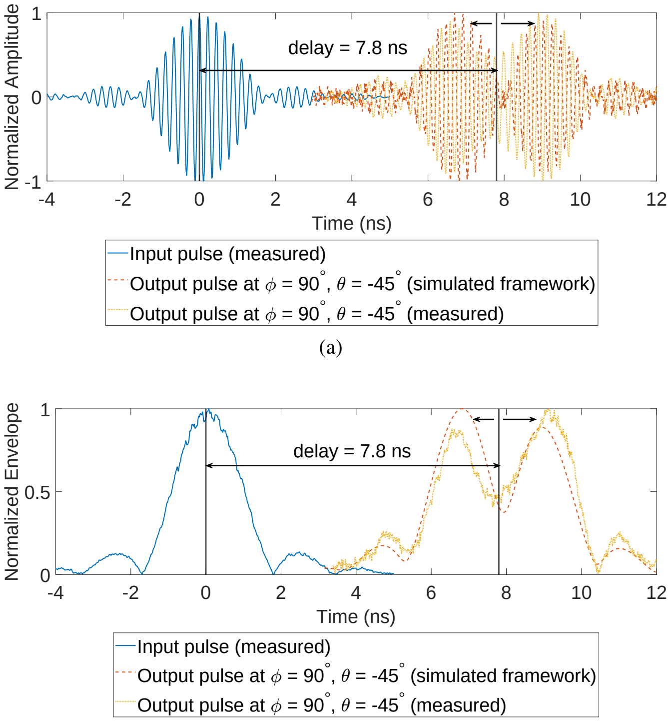

(a)

(b)

Fig. 10. (a) Normalized amplitude and (b) normalized envelope of the measured input pulse versus the simulated and measured output pulse with pulse distortion at ϕ = 90°, θ = -45°, with markers showing the 7.8 ns delay, corresponding with the 2.34 m distance between the antennas, and the time shift for the peak of the pulse envelope due to pulse distortion.

A thorough analysis is given in this section to explain the output pulse deformation more in detail. A cross-section of the yz-plane with the monopolar spline antenna and metal plate at $\phi = 90°$ and $\theta = -45°$ is shown in Fig. 11.

Due to the extra path length in the reflected path, the pulse contribution via the reflected path has a slightly larger delay than the direct pulse contribution, as shown in Fig. 12(a). The direct pulse in Fig. 12(a) is equal to the simulated output pulse along broadside and the reflected pulse is a time-shifted version of the simulated pulse along broadside, corresponding with the contribution of the reflected path. Adding the contributions of both paths leads to the normalized output pulse in Fig. 12(b), which resembles the normalized output pulse in Fig. 10(a). Finally, we compare the normalized envelope of the joint direct and reflected path, to the normalized envelope of the simulated and measured output pulse with pulse distortion at $\phi = 90°$, $\theta = -45°$ in Fig. 12(c). Note that, for all these results, the simulation framework is highly accurate for the time domain analysis of an antenna link. A very good agreement is found between simulated and measured time domain characteristics, such as SFF, DEE and pulse distortion, with and without the presence of an integration platform. The same analysis also applies to the output pulse at $\theta = 50°$ and at $\theta = -50°$ in the xz-plane.

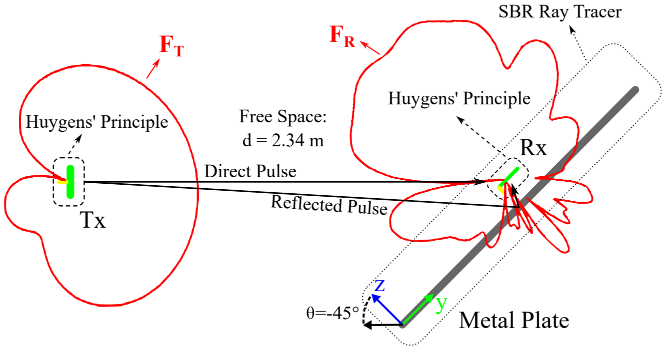

Fig. 11. Cross-section of the setup in the yz-plane at θ = -45° with $\mathbf{F}_T$ and $\mathbf{F}_R$ the simulated radiation vector of the transmit and receive antenna, respectively.

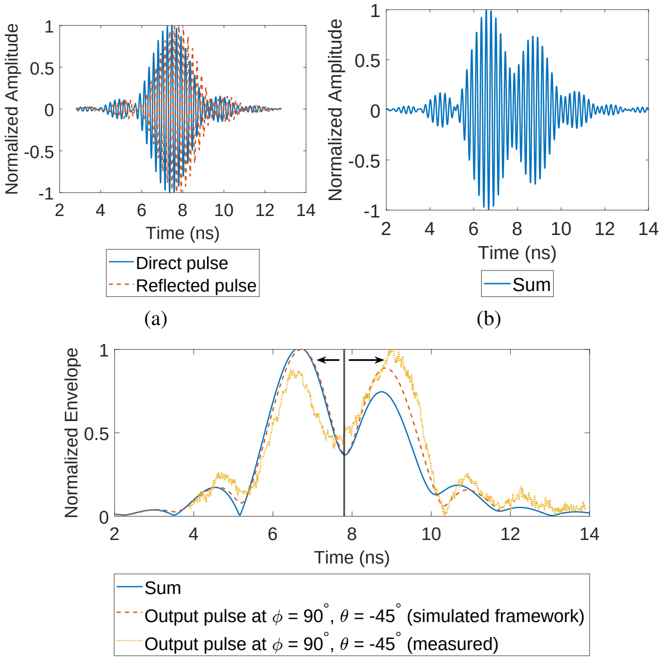

(a)

(b)

(c)

Fig. 12. Origins of the deformation of the output pulse with pulse distortion at $\phi = 90°$, $\theta = -45°$: (a) normalized amplitude of the direct pulse and the reflected pulse, (b) normalized amplitude of the sum of the direct pulse and the reflected pulse and (c) normalized envelope of the sum compared to the simulated and measured output pulse with pulse distortion at $\phi = 90°$, $\theta = -45°$, with markers showing the time shift for the peak of the pulse envelope due to pulse distortion.

E. Phase-Center Variation

In Fig. 8, both the measured and simulated DEE yielded a value of about 15 cm at $\phi = 90°$ and $\theta = 50°$, whilst the SFF for this angle was about 95%. This proves that the large ranging error at this angle results from an undesired phase-center variation, which can be clearly seen in Fig. 13. The output pulse at an angle of $\theta = 50°$ in the yz-plane closely resembles the pulse shape in the broadside direction, but a time shift of 0.5 ns is causing a DEE of 15 cm for a wave travelling at the speed of light in free space. This is why it is very important to take the DEE into account during the antenna optimization process, and not only the SFF, which is a largely used standard nowadays when designing UWB antennas. The accuracy of the proposed simulation framework is shown in Fig. 13, with the simulation framework being able to simulate this phase-center variation very accurately as well.

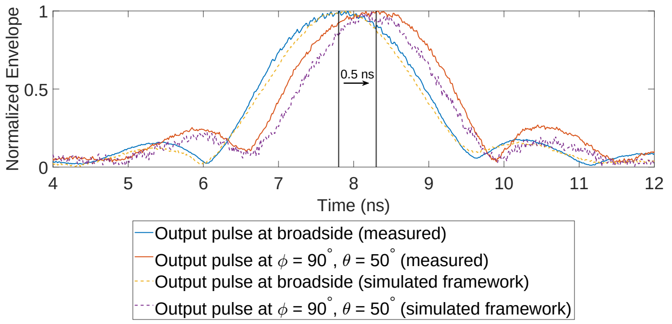

Fig. 13. Normalized measured and simulated envelope of the output pulse at broadside, and the output pulse with phase-center variation at $\phi = 90°$, $\theta = 50°$.

F. Benchmarking

To conclude this section, Table II provides a summary of the CPU times required to simulate the orientation-specific frequency and time-domain system-level metrics (SFF and DEE) for the setup described in Subsection IV-A by means of the proposed simulation framework versus two-port full-wave and ray-tracing simulations in CST Microwave Studio, using an Intel Core i7-10850H 2.70 GHz CPU with 16 GB RAM. The CST MWS full-wave solver only simulates and computes one antenna orientation at a specified distance at a time and, hence, does not scale well when additional orientations or distances need to be simulated. The CST MWS shooting and bouncing rays (SBR) ray-tracing requires a single full-wave simulation of each antenna in free space but also requires the antenna designer to manually rotate the antenna for every orientation. This makes such a ray-tracing solver a lot faster than the full-wave simulator, but this technique also does not scale well when additional orientations or distances need to be simulated, as shown in Table II.

TABLE II
SUMMARY OF CPU TIMES FOR THE FULL-WAVE SOLVER, SHOOTING AND BOUNCING RAYS (SBR) RAY-TRACING SOLVER AND OUR SIMULATION FRAMEWORK.

	CST MWS Full-Wave	**CST MWS SBR**	**Simulation Framework**
Free Space (2.34 m)			
Broadside	48min26s	4min43s	5min46s
2D plane [step 5°]	>2 days[1]	13min[1]	6min32s
2D plane [step 1°]	>12 days[1]	46min36s[1]	8min25s
Metal Plate Integration (2.34 m)			
Broadside	>1 hour	5min26s	7min50s
2D plane [step 5°]	>3 days[1]	>1 hour[1]	9min39s
2D plane [step 1°]	>16 days[1]	>5 hours[1]	14min55s

[1] Linearly extrapolated, rotation of the antenna model under test required for every step in CST Microwave Studio.

The proposed simulation framework computes the required system-level parameters for all requested orientations and distances in one simulation run. The simulation in broadside (5min46s) includes the full-wave simulation of both antennas separately and the time to calculate everything in Matlab. For multiple angles, the simulation time is only slightly affected by the number of orientations or distances between the antennas because of the modular approach, proposed in Fig. 1.

A CST MWS full-wave simulation, of the antennas used in this representative UWB link, has an average CPU load of 70% of the 6 cores of the Intel Core i7-10850H 2.70 GHz and an average memory load of 30% of the available 16 GB RAM, while a CST MWS SBR simulation has a reduced CPU and memory load of 30% and 10%, respectively. The modular approach in the proposed simulation framework enables a more efficient usage of the CPU and memory, minimizing the intensive full-wave simulations in combination with an efficient Matlab program, with a CPU and memory load of only 20% and 30%, respectively, to calculate the post-integration antenna-specific parameters and orientation-specific system-level figures of merit. As a result, this simulation framework provides the required speed and accuracy for the design and optimization of integrated IoT nodes for UWB localization and sensing applications.

V. APPLICATIONS: UWB TRANSCEIVER IMPERFECTIONS AND ROBOTIC INTEGRATION PLATFORMS

A. Two Way Ranging (TWR)

In the previous section, the DEE was studied to analyze the antenna-induced angle-dependent ranging bias, due to pulse distortion and/or phase-center variations. Now, a real UWB system is evaluated in terms of ranging accuracy using the same setup as presented in Fig. 5 with a Wi-PoS hardware platform connected to both the transmit and receive antenna [59]. The Wi-PoS hardware is configured to operate within the IEEE 802.15.4-2020 channel 3 frequency band [46]. To analyze the system's performance, the output pulse of the Wi-Pos board was measured in the time domain with a LabMaster 10-65Zi-A RTO from Teledyne LeCroy and in the frequency domain with a Rohde & Schwarz FS40 Spectrum Analyzer (SA), yielding Fig. 14. The transmit spectrum of the channel 3 output pulse, plotted in Fig. 14(b), is fully compliant with the spectral mask defined by the IEEE 802.15.4-2020 standard [46].

In order to accurately simulate this real UWB system, the measured pulse from the Wi-Pos board, plotted in Fig. 14(a), is

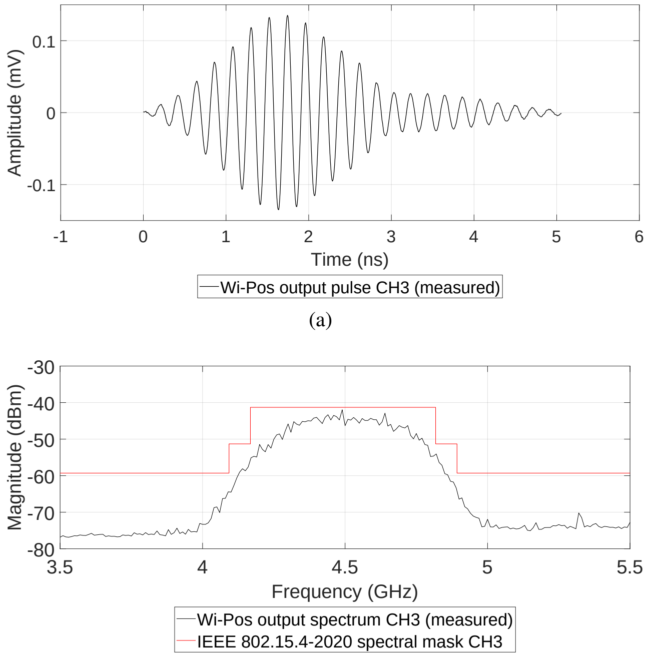

(a)

(b)

Fig. 14. Wi-Pos measured output pulse shape in channel 3: (a) time domain and (b) frequency domain.

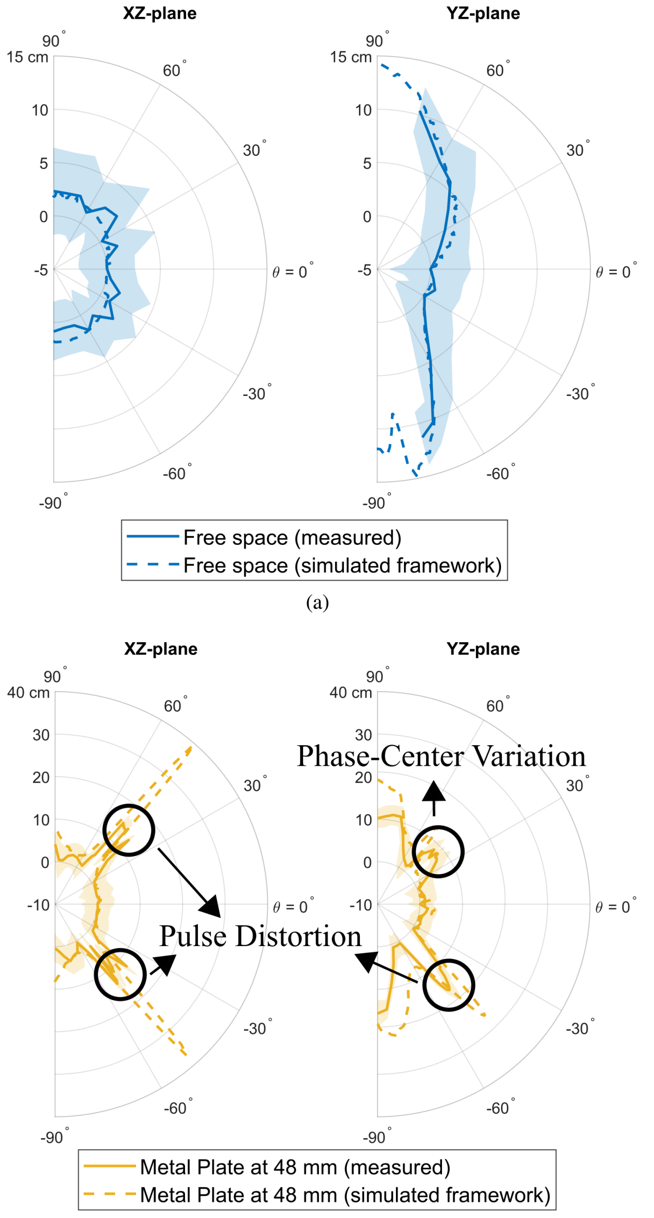

(a)

(b)

Fig. 15. Mean value (simulated and measured) and standard deviation (represented using a lighter color tone) of the TWR distance estimation error compared to broadside within the IEEE 802.15.4-2020 channel 3 frequency band, measured over a time period of 30s, for both the xz-plane (ϕ = 0°) and yz-plane (ϕ = 90°): (a) in free-space and (b) 48 mm in front of a metal plate.

now applied as the input pulse in the simulation framework. In addition, the non-linear characteristics of the RF front-end of Qorvo's DW1000 can lead to a range-bias effect that is related to the received signal level [60]. These data, provided by the manufacturer, were imported into the simulation framework. By interpolating between these RF front-end, the simulation framework is able to predict the DEE in the presence of these non-linear effects.

Therefore, for each angle in the xz-plane ($\phi = 0°$) and yz-plane ($\phi = 90°$), 200 TWR measurements were performed and averaged. The mean value and standard deviation of these measurements are plotted in Fig. 15. The measured results in free-space, shown in Fig. 15(a), match the results in Fig. 8, with sub-cm accuracy in the entire xz-plane. The inclusion of the non-linear behavior of the RF front-end into the simulation framework has no significant impact on the DEE in the xz-plane. Yet, the results for the yz-plane in free-space exhibit some deviations from the results in Fig. 8, with an increase in the TWR distance estimation error from +30° to +75° and from -30° to -75° in both the measurement and simulation. This is because the torus-shaped radiation pattern of the monopolar spline antenna leads to a lower received signal level, which results in an extra range bias [60].

Next, when comparing the measured results when deployed in front of the metal plate, depicted in Fig. 15(b), to the results in Fig. 8, a good agreement is found for the angles that were labeled ”Pulse Distortion” and the angle that was labeled ”Phase-Center Variation”. In the xz-plane, the same increase in ranging bias is noticed at +50° and -50° in the measurement as in the simulation with the RF front-end included. In contrast to the single narrow peaks in Fig. 8, the measured ranging bias now occurs for multiple angles between ±40° and ±50°, which is also well predicted after including the RF front-end in the simulation framework. In the yz-plane, a similar increase in measured ranging bias is noticed at -45°, where pulse distortion occurs. Furthermore, the angle labeled ”Phase-Center Variation” at +45°, is slightly shifted to a lower angle in the measurement results, but also shows a less prominent ranging error, which is expected from the results in Fig. 8. The simulated results for both the xz-plane and yz-plane exhibit a higher DEE for the angles that were labeled ”Pulse Distortion”, because, in practice, nulls in the radiation pattern are less prominent than in simulations. In general, it can be stated that the measured TWR distance estimation results are in very good agreement with the new simulation results, predicted by our simulation framework.

B. Integration on a Robotic Platform

In the previous section, a first representative UWB link was extensively validated in both the frequency and time domains to validate the proposed simulation framework. Industry 4.0 applications, such as smart factories, heavily rely on high-accuracy and autonomous robotic localization systems [61]. Therefore, a real robotic platform, being a TurtleBot3 Burger Mobile Robot (Fig. 16), is now considered as a practical application platform [62]. One of the innovative aspects of the simulation framework is the ability to simulate the impact of these larger and more complex integration platforms on the antenna link performance. Therefore, only a 3D CAD file and material parameters of the intended platform need to be imported in the proposed simulation framework.

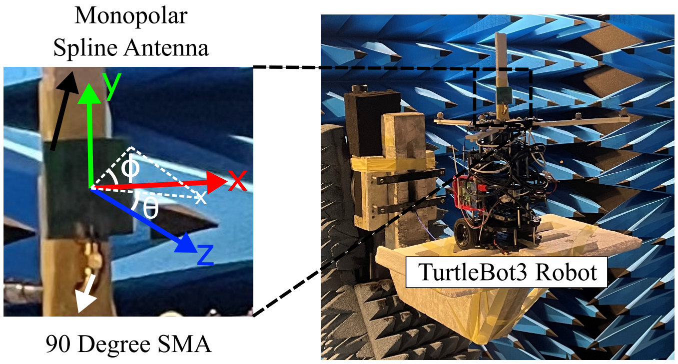

Fig. 16. Monopolar spline antenna placed on top of a TurtleBot3 Burger Mobile Robot.

The monopolar spline antenna was deployed 6 cm above the TurtleBot3 Burger Mobile Robot, in order to place the connector and measurement cable, and a coupled half-mode cavity-backed slot SIW antenna was exploited as the fixed transmit antenna. Otherwise, the same measurement configuration was maintained as in the previous section.

The simulated and measured SFF of the antenna link with the robot, as a function of θ, is shown in Fig. 17. Now, the full xz-plane ($\phi = 0°$) is depicted in combination with the top hemisphere of the yz-plane ($\phi = 90°$), since the robot is located below the monopolar spline antenna. The SFF characteristic in the full xz-plane is fairly constant, being higher than 90% for all values of θ. Since the robotic platform is placed in the null of the radiation pattern, this result is expected. In the yz-plane, there is a dip around 75° in the simulated and measured SFF data, due to the presence of the TurtleBot3 Burger Mobile Robot below the monopolar spline antenna in combination with the torus-shaped radiation pattern. The dip is more prominent in the SFF curve obtained with the simulation framework than in the measured SFF curve. This is because, in practice, nulls in the measured radiation pattern are less prominent than in the simulations, due to some finer and more detailed features that are not included in the simplified simulation model and because of measurement noise. In addition, a small angular shift is seen in the measured SFF curve, which is probably due to a simplified representation of the TurtleBot3 Burger Mobile Robot, as well as some small misalignment errors, in the simulation framework. Similar to the previous section, the simulation framework results of the SFF are in excellent agreement with the measurement results.

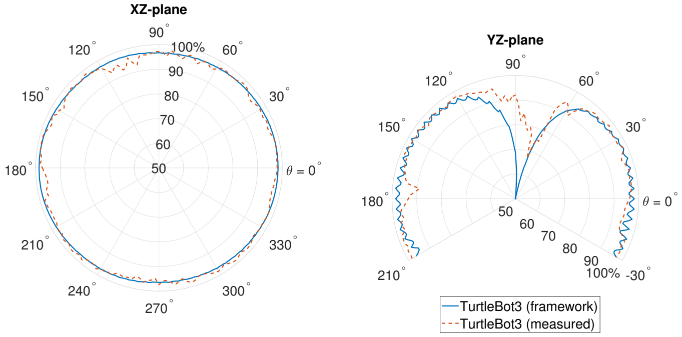

Fig. 17. Simulated and measured SFF on top of a TurtleBot3 robot in % for the xz-plane ($\phi = 0°$) and yz-plane ($\phi = 90°$).

VI. CONCLUSION

A novel simulation framework was presented to accelerate the design of active UWB antenna systems that satisfy the stringent requirements of demanding next-generation IoT applications and maintain performance when deployed in harsh and challenging environments. Particular attention was given to the integration of standalone simulation results into a system-level simulation framework, thereby facilitating lightweight simulations with excellent design flexibility. Moreover, this simulation framework is the first to include the Huygens' field equivalence principle to efficiently model the entire system environment, crucial to ensure high performance UWB antenna systems for integrated IoT applications. To obtain high accuracy with significantly reduced computational resources, the antenna link was partitioned, enabling the combination of standalone full-wave antenna simulations with different wireless channel models to construct the two-port antenna link.

The system was jointly characterized in the frequency, time and space domains, enabling the assessment and optimization of its system-level performance in terms of the SFF and DEE. The proposed simulation framework was validated by a series of time domain measurements, transmitting and measuring pulses in an anechoic chamber with an AWG and RTO, respectively. A good agreement between simulation and measurement results was observed for different antenna links. Furthermore, the simulation framework performance was benchmarked against commercial solvers, showing a reduction of the required CPU time by several orders of magnitude. Additionally, a practical application scenario was studied with a real robotic integration platform, proving good correspondence between simulation and measurement results.

This paper shows that the presence of an actual integration platform can drastically impact the system performance along different orientations. Moreover, the simulation and measurement outcomes emphasize the significance of the DEE for UWB ranging and sensing systems, highlighting that not only the SFF should be taken into account. The proposed simulation framework offers a solution for designers to analyze and optimize high–performance systems for these orientation-specific system-level metrics, such as the SFF and the DEE in full 3D, with the antenna integrated into the actual deployment platform.

REFERENCES

[1] A. Syberfeldt, M. Ayani, M. Holm, L. Wang, and R. Lindgren-Brewster, "Localizing Operators in the Smart Factory: A Review of Existing Techniques and Systems," *International Symposium on Flexible Automation, ISFA 2016*, pp. 179–185, 2016.

[2] B. J. Silva and G. P. Hancke, "Practical challenges of IR-UWB based ranging in harsh industrial environments," *Proceeding - 2015 IEEE International Conference on Industrial Informatics, INDIN 2015*, pp. 618–623, 2015.

[3] A. Rácz-Szabó, T. Ruppert, L. Bántay, A. Löcklin, L. Jakab, and J. Abonyi, "Real-Time Locating System in Production Management," *Sensors (Switzerland)*, vol. 20, no. 23, pp. 1–22, 2020.

[4] S. Jiang, M. J. Skibniewski, Y. Yuan, C. Sun, and Y. Lu, "Ultra-Wide Band Applications in Industry: A Critical Review," *Journal of Civil Engineering and Management*, vol. 17, no. 3, pp. 437–444, 2011.

[5] A. D. Preter, G. Goysens, J. Anthonis, J. Swevers, and G. Pipeleers, "Range Bias Modeling and Autocalibration of an UWB Positioning System," *2019 International Conference on Indoor Positioning and Indoor Navigation, IPIN 2019*, 2019.

[6] S. Bastiaens, J. Vanhie-Van Gerwen, N. Macoir, K. Deprez, C. De Cock, W. Joseph, E. De Poorter, and D. Plets, "Experimental Benchmarking of Next-Gen Indoor Positioning Technologies (Unmodulated) Visible Light Positioning and Ultra-Wideband," *IEEE Internet of Things Journal*, vol. 9, no. 18, pp. 17 858–17 870, 2022.

[7] A. Ghaffar, F. Khan, and S. H. Cho, "Hand Pointing Gestures Based Digital Menu Board Implementation Using IR-UWB Transceivers," *IEEE Access*, vol. 7, 2019.

[8] J. E. Kim, J. H. Choi, and K. T. Kim, "Robust Detection of Presence of Individuals in an Indoor Environment Using IR-UWB Radar," *IEEE Access*, vol. 8, pp. 108 133–108 147, 2020.

[9] Z. Duan and J. Liang, "Non-Contact Detection of Vital Signs Using a UWB Radar Sensor," *IEEE Access*, vol. 7, pp. 36 888–36 895, 2019.

[10] B. Silva and G. P. Hancke, "IR-UWB-Based Non-Line-of-Sight Identification in Harsh Environments: Principles and Challenges," *IEEE Transactions on Industrial Informatics*, vol. 12, no. 3, pp. 1188–1195, 2016.

[11] S. Yan, P. J. Soh, and G. A. Vandenbosch, "Wearable ultrawideband technology- A review of ultrawideband antennas, propagation channels, and applications in wireless body area networks," *IEEE Access*, vol. 6, pp. 42 177–42 185, 2018.

[12] P. P. Shome, T. Khan, A. A. Kishk, and Y. M. Antar, "Quad-Element MIMO Antenna System Using Half-Cut Miniaturized UWB Antenna for IoT-Based Smart Home Digital Entertainment Network," *IEEE Internet of Things Journal*, vol. 10, no. 20, pp. 17 964–17 976, 2023.

[13] G. Quintero, J. F. Zurcher, and A. K. Skrivervik, "System Fidelity Factor: A New Method for Comparing UWB Antennas," *IEEE Transactions on Antennas and Propagation*, vol. 59, no. 7, pp. 2502–2512, 2011.

[14] Q. Van Den Brande, S. Lemey, and H. Rogier, "Planar Sectoral Antenna for IR-UWB Localization with Minimal Range Estimation Biasing," *IEEE Antennas and Wireless Propagation Letters*, vol. 20, no. 2, pp. 135–139, 2021.

[15] T. Cuyckens and H. Rogier, "Framework for the Simulation of Wireless Power Transmissions over Ultra Wide Band Links in Multipath Propagation Environments in the Vicinity of the Human Body," *International Journal of Numerical Modelling*, vol. 29, no. May 2015, pp. 364–379, 2016.

[16] D. Veit, M. Gadringer, and E. Leitgeb, "On UWB Pulse Distortion Caused by Amplifiers and Mismatched Antennas," *2020 IEEE MTT-S International Conference on Microwaves for Intelligent Mobility, ICMIM 2020*, 2020.

[17] X. Qing, Z. N. Chen, and M. Y. W. Chia, "Characterization of ultrawideband antennas using transfer functions," *Radio Science*, vol. 41, no. 1, pp. 1–10, 2006.

[18] E. Pancera, T. Zwick, and W. Wiesbeck, "Spherical Fidelity Patterns of UWB Antennas," *IEEE Transactions on Antennas and Propagation*, vol. 59, no. 6 PART 2, pp. 2111–2119, 2011.

[19] S. Pancrazio, P. Nguyen, S. Wagner, A. Hossain, and A. V. Pham, "Digital Pre-Distortion to Correct UWB Pulses in a Boresight Test," *2021 IEEE International Symposium on Antennas and Propagation and North American Radio Science Meeting, APS/URSI 2021 - Proceedings*, pp. 525–526, 2021.

[20] T. Liu, B. Li, and L. Yang, "Phase Center Offset Calibration and Multipoint Time Latency Determination for UWB Location," *IEEE Internet of Things Journal*, vol. 9, no. 18, pp. 17 536–17 550, 2022.

[21] M. R. Mahfouz, C. Zhang, B. C. Merkl, M. J. Kuhn, and A. E. Fathy, "Investigation of High-Accuracy Indoor 3-D Positioning Using UWB Technology," *IEEE Transactions on Microwave Theory and Techniques*, vol. 56, no. 6, pp. 1316–1330, 2008.

[22] N. Kumar, O. Chukwuka, and D. Seetharamdoo, "Integration of Antennas for Communication System on Complex Platforms," *Lecture Notes in Computer Science (including subseries Lecture Notes in Artificial Intelligence and Lecture Notes in Bioinformatics)*, vol. 12574 LNCS, pp. 125–136, 2020.

[23] V. Sipal, M. John, D. Neirynck, M. McLaughlin, and M. Ammann, "Advent of practical UWB localization: (R)Evolution in UWB antenna research," *8th European Conference on Antennas and Propagation, EuCAP 2014*, pp. 1561–1565, 2014.

[24] V. Niculescu, D. Palossi, M. Magno, and L. Benini, "Energy-Efficient, Precise UWB-Based 3-D Localization of Sensor Nodes With a Nano-UAV," *IEEE Internet of Things Journal*, vol. 10, no. 7, pp. 5760–5777, 2023.

[25] Q. Van Den Brande, S. Lemey, J. Vanfleteren, and H. Rogier, "Highly Efficient Impulse-Radio Ultra-Wideband Cavity-Backed Slot Antenna in Stacked Air-Filled Substrate Integrated Waveguide Technology," *IEEE Transactions on Antennas and Propagation*, vol. 66, no. 5, pp. 2199–2209, 2018.

[26] G.-J. Gordebeke, S. Lemey, O. Caytan, M. Boes, J. Jocqué, S. Van de Velde, C. Marshall, E. De Poorter, and H. Rogier, "Time-Domain-Optimized Antenna Array for High-Precision IR-UWB Localization in Harsh Urban Shipping Environments," *IEEE Sensors Journal (Early Access)*, 2023.

[27] M. J. Kuhn, M. R. Mahfouz, C. Zhang, B. C. Merkl, and A. E. Fathy, "A System-Level Simulation Framework for UWB Localization," *IEEE Transactions on Microwave Theory and Techniques*, vol. 58, no. 12 PART 1, pp. 3527–3537, 2010.

[28] M. Demirkan and R. R. Spencer, "Antenna Characterization Method for Front-End Design of Pulse-Based Ultrawideband Transceivers," *IEEE Transactions on Antennas and Propagation*, vol. 55, no. 10, pp. 2888–2899, 2007.

[29] D. Sarkar, T. Khan, Jayadeva, and A. A. Kishk, "Machine Learning Assisted Hybrid Electromagnetic Modeling Framework and its Applications to UWB MIMO Antennas," *IEEE Access*, vol. 11, no. December 2022, pp. 19 645–19 656, 2023.

[30] A. O. Boryssenko and D. H. Schaubert, "Antenna Link Transfer Function Factorization Applied to Optimized Channel Design," *IEEE Transactions on Antennas and Propagation*, vol. 54, no. 10, pp. 2878–2889, 2006.

[31] A. Sibille, "A framework for analysis of antenna effects in UWB communications," *IEEE Vehicular Technology Conference*, vol. 61, no. 1, pp. 48–52, 2005.

[32] Y. Duroc, A. Ghiotto, T. P. Vuong, and S. Tedjini, "UWB Antennas: Systems With Transfer Function and Impulse Response," *IEEE Transactions on Antennas and Propagation*, vol. 55, no. 5, pp. 2006–2008, 2007.

[33] A. E. C. Tan, M. Y. W. Chia, K. K. M. Chan, and K. Rambabu, "Modeling the Transient Radiated and Received Pulses of Ultra-Wideband Antennas," *IEEE Transactions on Antennas and Propagation*, vol. 61, no. 1, pp. 338–345, 2013.

[34] M. Mudroch, P. Cerny, P. Hazdra, and M. Mazanek, "UWB dipole antenna optimization with neural network tuned algorithm," *European Conference on Antennas and Propagation, EuCAP 2009, Proceedings*, pp. 1491–1494, 2009.

[35] S. Chamaani, S. A. Mirtaheri, and M. S. Abrishamian, "Improvement of time and frequency domain performance of antipodal Vivaldi antenna using multi-objective particle swarm optimization," *IEEE Transactions on Antennas and Propagation*, vol. 59, no. 5, pp. 1738–1742, 2011.

[36] M. J. Kuhn, C. Zhang, S. Lin, M. R. Mahfouz, and A. E. Fathy, "A system level design approach to UWB localization," *IEEE MTT-S International Microwave Symposium Digest*, pp. 1409–1412, 2009.

[37] Y. Wang, M. J. Kuhn, M. R. Mahfouz, and A. E. Fathy, "A comprehensive system-level simulation paradigm for UWB systems," *2010 IEEE International Symposium on Antennas and Propagation and CNC-USNC/URSI Radio Science Meeting - Leading the Wave, AP-S/URSI 2010*, pp. 1–4, 2010.

[38] Y. Wang and A. E. Fathy, "Advanced system level simulation platform for three-dimensional UWB through-wall imaging sar using time-domain approach," *IEEE Transactions on Geoscience and Remote Sensing*, vol. 50, no. 5 PART 2, pp. 1986–2000, 2012.

[39] WIPL-D, "WIPL-D Electromagnetic Simulation Software - Products Overview," https://wipl-d.com/, 2024.

[40] D. Systèmes, "CST Studio Suite," https://www.3ds.com/products/simulia/cst-studio-suite, 2024.

[41] D. Sarkar, T. Khan, F. A. Talukdar, and Y. M. Antar, "Computational intelligence paradigms for UWB antennas: a comprehensive review of analysis, synthesis and optimization," *Artificial Intelligence Review*, vol. 56, no. 1, pp. 655–684, 2023. [Online]. Available: https://doi.org/10.1007/s10462-022-10181-w

[42] Q. Wu, H. Wang, and W. Hong, "Multistage Collaborative Machine Learning and its Application to Antenna Modeling and Optimization," *IEEE Transactions on Antennas and Propagation*, vol. 68, no. 5, pp. 3397–3409, 2020.

[43] B. Zhang, C. Jin, K. Cao, Q. Lv, and R. Mittra, "Cognitive Conformal Antenna Array Exploiting Deep Reinforcement Learning Method," *IEEE Transactions on Antennas and Propagation*, vol. 70, no. 7, pp. 5094–5104, 2022.

[44] M. Koohestani, A. A. Moreira, and A. K. Skrivervik, "Fidelity concepts used in UWB systems," *IEEE Antennas and Propagation Society, AP-S International Symposium (Digest)*, pp. 824–825, 2014.

[45] D. M. Pozar, *Microwave engineering; 4th ed.* Hoboken, NJ: Wiley, 2011.

[46] "IEEE Standard for Low-Rate Wireless Networks - Redline," *IEEE Std 802.15.4-2020 (Revision of IEEE Std 802.15.4-2015) - Redline*, pp. 1–1294, 2020.

[47] Recommendation ITU-R, "Measurement Techniques of Ultra-Wideband Transmissions," 2006.

[48] G. Singh, E. Allebes, Y. He, E. Tiurin, P. Mateman, J. F. Dijkhuis, G. J. Van Schaik, E. Bechthum, J. Van Den Heuvel, M. El Soussi, A. Breeschoten, H. Korpela, G. J. Gordebeke, S. Lemey, C. Bachmann, and Y. H. Liu, "An IR-UWB IEEE 802.15.4z Compatible Coherent Asynchronous Polar Transmitter in 28-nm CMOS," *IEEE Journal of Solid-State Circuits*, vol. 56, no. 12, pp. 3799–3810, 2021.

[49] G. Lee, J. Jang, J. H. Kim, and T. W. Kim, "An IR-UWB CMOS Transceiver With Extended Pulse Position Modulation," *IEEE Journal of Solid-State Circuits*, vol. 57, no. 8, pp. 2281–2291, 2022.

[50] Y. T. Lo and S. W. Lee, *Antenna Handbook, Theory, Applications, and Design*. Van Nostrand Reinhold, 1988.

[51] P.-S. Kildal, "Equivalent circuits of receive antennas in signal processing arrays," *Microwave and Optical Technology Letters*, vol. 21, pp. 244–246, 1999.

[52] M. Rütschlin and D. Tallini, "Simulation for Antenna Design and Placement in Vehicles," *IET Seminar Digest*, vol. 2017, no. 1, 2017.

[53] C. A. Balanis, *Antenna theory: analysis and design*. Wiley-Interscience, 2005.

[54] M.-K. Li and W. C. Chew, "Wave-Field Interaction With Complex Structures Using Equivalence Principle Algorithm," *IEEE Transactions on Antennas and Propagation*, vol. 55, no. 1, pp. 130–138, 2007.

[55] J. M. Rutherford and W. C. Chew, "Generalized Solver Hybridization Using Equivalence Principle Algorithm," *IEEE Transactions on Antennas and Propagation*, vol. 68, no. 3, pp. 2206–2212, 2020.

[56] M. S. Tasic and B. M. Kolundzija, "Method of Moment Weighted Domain Decomposition Method for Scattering From Large Platforms," *IEEE Transactions on Antennas and Propagation*, vol. 66, no. 7, pp. 3577–3589, 2018.

[57] L. Li, J. Pan, C. Hwang, G. Cho, H. Park, Y. Zhang, and J. Fan, "Near-field coupling estimation by source reconstruction and Huygens's equivalence principle," *2015 IEEE Symposium on Electromagnetic Compatibility and Signal Integrity, EMCSI 2015*, pp. 324–329, 2015.

[58] I. P. Guembe, P. Lopez-Iturri, H. Klaina, G. G. Ezker, F. S. De Jauregui Urdanoz, J. L. Z. Cestau, L. Azpilicueta, and F. Falcone, "Wireless Characterization and Assessment of an UWB-Based System in Industrial Environments," *IEEE Access*, vol. 9, pp. 107 824–107 841, 2021.

[59] B. Van Herbruggen, B. Jooris, J. Rossey, M. Ridolfi, N. Macoir, Q. Van den Brande, S. Lemey, and E. De Poorter, "Wi-PoS : a Low-Cost, Open Source Ultra-Wideband (UWB) Hardware Platform with Long Range Sub-GHz Backbone," *SENSORS*, vol. 19, no. 7, p. 16, 2019.

[60] Decawave, "Sources of Error in DW1000 Based Two-Way Ranging (TWR) Schemes," pp. 1–21, 2014.

[61] S.-H. Bach, P.-B. Khoi, and S.-Y. Yi, "Global UWB System: A High-Accuracy Mobile Robot Localization System With Tightly Coupled Integration," *IEEE Internet of Things Journal*, pp. 1–1, 2024.

[62] TurtleBot, "Turtlebot3," https://emanual.robotis.com/docs/en/platform/turtlebot3/overview/, 2023.